Landsc Ecol (2023) 38:169–183
https://doi.org/10.1007/s10980-022-01540-7

RESEARCH ARTICLE

Prolonged coastal inundation detected with synthetic aperture radar significantly retarded functional recovery of mangroves after major hurricanes

Mei Yu · Qiong Gao

Received: 26 July 2022 / Accepted: 29 September 2022 / Published online: 18 October 2022

Abstract
Context Hurricanes are major threats to coastal mangrove ecosystems. Inundation has been implicitly reported to associate with mangrove damages and mortality. However, there have been no spatial statistical analyses of the impact of inundation on mangrove recovery at landscape scales.
Objectives Our objectives are to detect spatiotemporal patterns of inundation after major hurricanes and to explore explicitly the role of inundation in mangrove recovery at landscape scale.
Methods Using C-band Synthetic Aperture Radar images, we detected the spatiotemporal pattern of surface flood and derived the spatial distribution of inundation depth under mangrove canopies based on surrounding surface flood and elevation along northern Puerto Rico coasts after major hurricanes in 2017. Based on the Enhanced Vegetation Index, we derived the short-term hurricane impact and the recovery ratio from 2018 to 2021, and analyzed the impact and the recovery of mangrove greenness by means of spatial error models.
Results The identification of surface flood reached very high accuracy. The severe impact is significantly explained by greater gust windspeed during the hurricane and lower elevation. More importantly, retarded mangrove greenness recovery is significantly explained by severer impacts, longer and deeper inundation, and heavier hurricane rainfall.
Conclusions Spatiotemporal heterogeneity in flood depth plays a significant and essential role in mangrove recovery and delayed mortality after major hurricanes. The derived flood depth turns out to be a better explanator of mangrove recovery than elevation, which highlights importance of landscape hydrology and topography with respect to mangrove response and restoration after major hurricanes.

Keywords Inundation · Coastal wetlands · Hurricane · SAR · Flooding detection · Caribbean

Introduction

Mangrove forests provide essential ecosystem services of water purification, flood mitigation, fisheries, carbon sequestration, and erosion protection for coastal communities (Costanza et al. 2008; Barbier et al. 2011; Gedan et al. 2011). Yet coastal mangroves are facing great anthropogenic threats of deforestation for coastal development, agriculture, and urbanization (Dahl and Stedman 2013), as well as natural threats of rising sea level (Kirwan and Megonigal 2013;

Supplementary Information The online version contains supplementary material available at https://doi.org/10.1007/s10980-022-01540-7.

M. Yu (✉) · Q. Gao
Department of Environmental Sciences, University of Puerto Rico, Rio Piedras, San Juan, PR 00926, USA
e-mail: meiyu@ites.upr.edu

Anderson et al. 2022), more frequent and intensive tropical cyclones disturbance (Imbert 2018; Sippo et al. 2018; Patrick et al. 2020), and longer period of droughts (Duke et al. 2017). Therefore, the sustainable ecosystem services of coastal mangroves bear great uncertainty.

Tropical cyclones and climate extremes are main natural causes for mangrove diebacks and mortality (Sippo et al. 2018; Taillie et al. 2020). Globally, about 36,000 ha of mangroves died since 1960s, and half of the reported mangrove area loss due to natural causes were attributed to tropical cyclones (Sippo et al. 2018). Recently, climate extremes such as lengthy drought and heat wave were found to incur mass mangrove dieback in Northern Australia (Duke et al. 2017). In the Caribbean, hurricanes (Wadsworth and Englerth 1959; Gao and Yu 2022) and hypersaline conditions caused mangrove mortality (Jimenez et al. 1985; Sippo et al. 2018).

In addition to the immediate damages and mortality such as defoliation, snapping branch/stem, and uprooting trunks by hurricane winds (Han et al. 2018; Taillie et al. 2020; Gao and Yu 2021b), widespread coastal inundations have been reported due to compound flooding of oceanic, fluvial, and pluvial sources (Patrick et al. 2020; Ye et al. 2021), and the prolonged inundations may cause delayed mortality as excessive stagnant water and/or associated sediment deposits may immerse or bury aerial roots and suffocate the mangroves (Ellison 1999; Lewis et al. 2016; Radabaugh et al. 2020). In the Lower Florida Keys, mangrove mortality assessed 9-month after a major hurricane in 2017 was almost doubled of that found 2–3 months after the hurricane, i.e., 36.6% versus 18.6%, and the excessive mud deposits was identified as a causal factor to smother aerial roots to suffocate the mangroves (Radabaugh et al. 2020). Severe mangrove canopy damage was found in the areas with high storm surge or inland site with poor drainage capacity (Lagomasino et al. 2021).

In the Caribbean, the severe damage of mangrove canopies by major hurricanes in 2017 was found in the area prone to inundation (Yu and Gao 2020b; Gao and Yu 2022). The impact of inundation-related factors has been statistically revealed in the analysis of mangrove dieback and recovery at both patch and landscape scales. In a multi-patch study, coastal mangroves experienced the greatest impact and the slowest yet latest recovery with a one-year relative recovery of 0.44 compared to a recovery ratio greater than 0.70 for upland forests (Yu and Gao 2020b). Greater impact on mangroves was significantly associated with higher rainfall and lower slope, and the mangrove recovery was mostly limited by inundation-related factors such as elevation, slope, and drainage capacity. Particularly, mangrove recovery is facilitated by river presence, i.e., better drainage, which explained 65% variation in one-year recovery ratio. At landscape scales, the analyses on the reduction of canopy height due to major hurricanes revealed that mangroves residing in low elevation and close to rivers or canals exhibited greater canopy damages (Gao and Yu 2021b). Multi-site studies showed that site with greater rainfall is associated with more canopy height reduction (Gao and Yu 2022).

Although the explanatory factors (rainfall, elevation, distance to canals, etc.) involved in above studies point to inundation which may be the variable directly leading to the spatial variation of delayed mortality (Radabaugh et al. 2020; Yu and Gao 2020b; Gao and Yu 2021b, 2022; Lagomasino et al. 2021), inundation has never been explicitly incorporated in landscape-level studies and therefore there is a gap in these studies and analyses which can explicitly address the essential role of inundation in damages and recovery of mangroves at landscapes. An important reason for this knowledge gap is the difficulty in monitoring inundation under mangroves.

Recent advances in remote sensing, especially the progresses in moderate-resolution synthetic aperture radar (SAR), makes it possible to monitor surface flood at high frequencies during natural disasters. Indeed, spaceborne and airborne remote sensing techniques have been used to monitor surface inundation at various scales from watershed to globe (Bartsch et al. 2009; Huang et al. 2014; Pekel et al. 2016; Cian et al. 2018b). For example, LiDAR and multi-temporal aerial images at 1-m resolution (NAIP, National Agriculture Imagery Program) were integrated to monitor the wetland surface inundation dynamics in the Prairie Pothole Region of North America at fine watershed scales (Wu et al. 2019). Three-million Landsat images were processed via the Google Earth Engine cloud platform to explore global surface water dynamics in 1984–2015 at moderate 30-m resolution (Pekel et al. 2016). Compared to the optical images, SAR images with the capacity to penetrate clouds provide all-weather flood monitoring (Veloso et al.

2017). SAR images are becoming more available in both great revisit frequency and high spatial resolution (Torres et al. 2012). For example, Sentinel-1 satellites provide the images every 6 days at 10-m spatial resolution. Change detection, thresholding, and classification are common techniques to detect flooding from radar images (Cian et al. 2018a; Clement et al. 2018). Supervised and unsupervised classifications have been used for flood mapping with applications in agriculture and disastrous response (Hosseini et al. 2020; Singha et al. 2020). Machine-learning techniques are also applied to rapid flood assessment (Huang et al. 2018; Jiang et al. 2021). Compared to detecting surface flood, assessment of flooding under dense vegetation canopy such as the mangroves is still difficult (Cian et al. 2018a).

The tropical island of Puerto Rico hosts large distributions of mangroves in its coastal plains, and the geographic setting in the northeastern tip of the Caribbean makes it prone to frequent tropical cyclone disturbances (López-Marrero et al. 2019). These conditions make the island an ideal "lab" to investigate the impacts of hurricanes on mangroves. While basin and riverine mangroves are mostly found on the northern coast, fringe and over-washed mangroves are usually found on the southern coast (Miller and Lugo 2009). Historically, mangroves in Puerto Rico declined from about 11,000 ha in 1800s to about 6000 ha in 1960s due to the expansions of agriculture and urban development (Martinuzzi et al. 2009). However, the wetland protection policies implemented after 1970s such as RAMSAR and US Clean Water Act led to the mangrove restoration to about 8000 ha in large, aggregated patches (Kennaway and Helmer 2007; Gao and Yu 2014). Mangrove encroachments into marshes due to saltwater intrusion were further detected during 2000–2010 (Yu et al. 2019). In September 2017, two consecutive major hurricanes brought furious winds and torrential rains to the island and induced mudslides/landslides (Hughes and Schulz 2020), flooding, and widespread damages to the coastal ecosystems (Taillie et al. 2020; Gao and Yu 2021b). Specifically, Hurricane Irma of category five passed by the northeast of the island on Sep. 6 with a sustaining wind of 298 km h^{-1}, and Hurricane Maria of high-end category four made a landfall at the southeast of the island on Sep. 20 with a sustaining wind of 249 km h^{-1}. The observed rainfall was as high as 965 mm (38 inches) and the storm surge combined with the tide made a maximum inundation level as high as 1.8–2.7 m (6–9 feet) in the east coast (Pasch et al. 2019). The scales of the hurricanes and the severity of disturbance have a frequency of approximately 1 in 100 years in Puerto Rico history.

This study addresses explicitly the essential role of spatiotemporal patterns of inundation in the impact and recovery of mangroves after major hurricanes at landscape scales. The objectives of this study are (1) to detect the spatiotemporal pattern of coastal surface inundation after major hurricanes in 2017 using SAR images, (2) to derive the flood under mangrove canopies based on the surrounding surface floods, and (3) to explore explicitly the role of derived inundation under canopies in mangrove damage and recovery after the major hurricanes. We used the high-frequency Sentinel-1 SAR images with moderate spatial resolution to detect the surface inundation with supervised classification, and then derived the inundation under the mangroves based on the surrounding surface flood and elevation profile. We hypothesized that the surface inundation after the major hurricanes would exhibit heterogeneity in both space and time, and the spatiotemporally heterogeneous mangrove recovery would be significantly inhibited by the inundation under canopies.

Methods

Study area

Puerto Rico is located in the northeastern Caribbean (Fig. 1, centered at 18°15′N and 66°30′W) and the main island has an area of around 8709 km^2. The coastline of Puerto Rico spans 800 km with the northern coast facing to the deep Atlantic Trench and the southern coast facing to the Caribbean Sea (Yu et al. 2019). The central mountain range, Cordillera Central running from east to west, divides the island into the windward north which receives annual rainfall up to more than 4000 mm, and the leeward south which receives around 1000 mm rainfall. The ample rainfall and strong tides make the northern coastal plains flatter and wider than those in the south. The island hosts vast distributions of palustrine and estuarine wetlands (Gao and Yu 2014). There are three true mangrove species in Puerto Rico, i.e., red mangrove (*Rhizophora mangle*), black mangrove (*Avicennia*

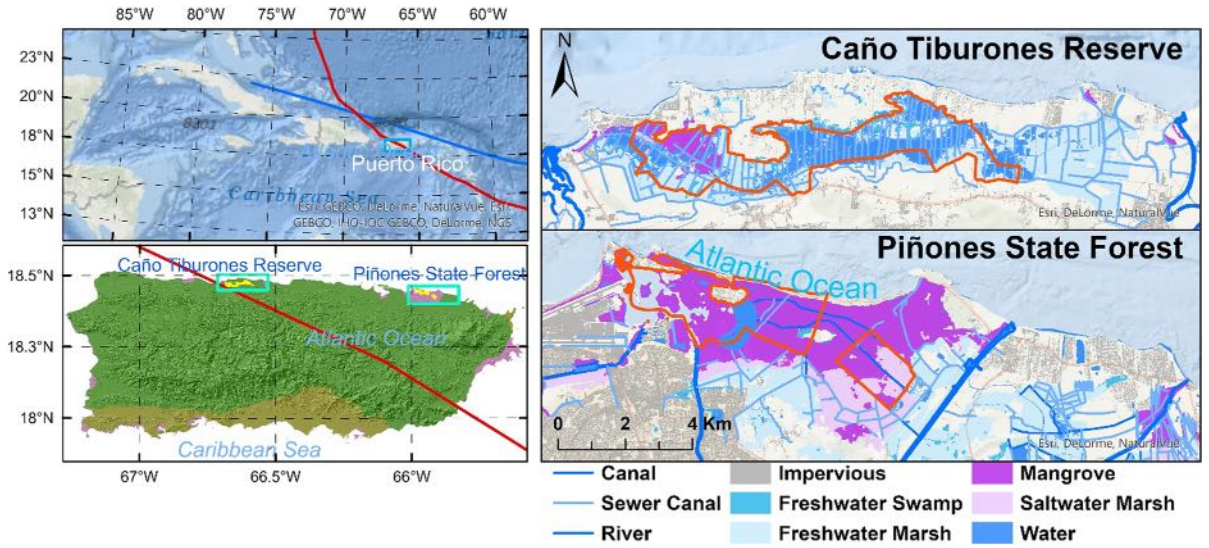

Fig. 1 Location of Puerto Rico in between the Atlantic Ocean and the Caribbean Sea (left), blue and red lines are the paths of Hurricane Irma (September 6, 2017) and Hurricane Maria (September 20, 2017), respectively; Wetland distribution in the largest mangrove forest of Piñones State Forest in the east and the largest emergent wetland of Caño Tiburones Reserve in the west (right)

germinans), and white mangrove (*Laguncularia racemosa*) (Miller and Lugo 2009; Quadros and Zimmer 2017). Red and black mangroves have a high tolerance to salinity, whereas white mangroves have a moderate tolerance (Lovelock et al. 2016). The spatial distribution of the three species depends on local topography and hydrology. Red mangroves with stilt roots live mostly near the coastal water or the verge of lagoons/river mouths. Black mangroves have long horizontal roots connecting numerous pneumatophores and live in shallow water or muddy soil environments. White mangroves usually grow in slightly higher, drier environments than black mangroves.

We selected the northern coastal plains as our study areas which host vast estuarine and palustrine wetlands and are close to the path of Hurricane Maria (Fig. 1). The Piñones State Forest in the northeast, around 1660 hectares, hosts the largest mangrove forest with the adjacent freshwater and saltwater marshes to the south and the southeast (Fig. 1). Estuarine wetlands dominate the protected area with 753 ha of mangroves. The elevation within the vegetative wetlands ranges from −0.6 to 12.8 m with a mean of 0.48 m and a standard deviation of 0.49 m. Quebrada Blasina in the southeast and several canals in the east and south of the Piñones lagoon provide freshwater and nutrients to the wetlands (Gao and Yu 2021b). The Caño Tiburones Reserve in the northwest, around 1550 ha, is one of the most extensive emergent wetlands with only 154 ha of mangroves. The elevation within the vegetative wetlands ranges from −0.1 to 4.3 m with a mean ± standard deviation of 0.35 ± 0.52 m. Canals of drainage within the reserve are intense, originally built to drain the sugarcane fields. Other major coastal wetlands along the northern coast are located at, from west to east, Tortuguero Lagoon, Cibuco Natural Reserve, Dorado, Toa Baja, Caño Martín Peña Natural Reserve, and Río Espíritu Santo Natural Reserve. The wetland within La Plata riverside in between Dorado and Toa Baja encountered the most severe flooding after the hurricanes (Pasch et al. 2019).

Data preparation

To assess the flooding in the coastal wetlands after the major hurricanes, we adopted the SAR images on-board the two Sentinel-1 satellites (Torres et al. 2012) sharing the same orbit plane but with a 180° orbital phasing difference. Each of the satellites carries a SAR instrument operating within C-band (5.405 GHz) and orbits with a 12-day repeat cycle.

For tropics, the two satellites make the images available every 6 days and due to the emergency response (www.esa.int/Applications/Observing_the_Earth/Copernicus/Sentinel-1/Emergency_response), the images acquired right after the major hurricanes are more than usual (Online Appendix Table). We used the Copernicus Sentinel-1 SAR data acquired under the Interferometric Wide swath (IW) mode designed for land monitoring. The images were preprocessed for thermal noise removal, radiometric calibration, and terrain correction to Level-1 ground range detected (GRD) format using the SNAP processing tool, a Sentinel-1 Toolbox provided by European Space Agency (ESA, sentinel.esa.int/web/sentinel/toolboxes/sentinel-1). We further improved the images by angular-based radiometric slope correction (volume model) (Hoekman and Reiche 2015; Vollrath and Mullissa 2020) based on the 10-m resolution DEM (Digital Elevation Model) available for the island.

We use Google Earth Engine platform for data retrieval, data preprocessing, and data analysis (Gorelick et al. 2017). Specifically, we collected the Sentinel-1 SAR images for two time periods, during flooding, i.e., Sep. 20–Sep. 30, and post-flooding, i.e., Oct. 1–Oct. 31, 2017, to detect spatiotemporal extent of inundation during the aftermath of the major hurricanes. We focus on the flooding during Sep. 20–Sep. 30 as the initial exploration of the images showed that the surface flooding largely vanished in October 2017. The major hurricanes caused drastic land surface modifications (Gao and Yu 2021b). Therefore, to identify the flooded areas, we used the images from Oct. 1 to Oct. 31, 2017 to create a reference image as the temporal median at each pixel. For each image during the flooding period (Sep. 20–Sep. 30, 2017), we calculated the Normalized Difference Flooding Index (NDFI) based on the radar backscatter to enhance the signal of flooding area (Cian et al. 2018a). NDFI is calculated as the normalized difference of backscatter between the reference image and each image acquired during the flooding event. We calculated two NDFI based on VV (vertical transmitting with vertical receiving) and VH (vertical transmitting with horizontal receiving) bands, respectively. Backscatter values in dB were converted to natural values before calculating the indices. Values at VH band can discriminate largely water from non-water pixels (Chen et al. 2017) and the ratio of VH and VV was proposed to be a more stable indicator as it reduces the effects of double bouncing and the errors related to the acquisition systems or the physical environment (Veloso et al. 2017). Therefore, the ratio was also added as an auxiliary variable for the detection of flooding (Veloso et al. 2017).

Detection of surface flood and derived flood under mangroves

Based on the radar backscatter signals during the flooding event and the reference period as well as the derived flooding indices, we identified surface flooded areas for each day with available SAR images during flooding by means of random forest (RF) classification (Breiman 2001). The features to train the random forest classifier included the bands of VV, VH, their ratio during the flooding events and during the reference period, respectively, and the NDFI based on VV and VH, respectively. Additionally, we incorporated a high-resolution DEM (10-m) and the derived slope as auxiliary features in the classification to quantify the role of topography in wetlands distribution and flooding identification. The training datasets for RF were delineated from high-resolution aerial photographs (Environmental Response Management Application—Caribbean, ERMA by NOAA and EPA) and images during and after the flooding, and included the classes of Flood, Permanent Water, Mangroves and associates, Marshes, Herbaceous Upland, Forested Upland, and Urban Cover. The high-resolution (2-m) land cover map provided by NOAA was also adopted as an important reference to identify different wetland types (Office for Coastal Management 2020). The classifier was rigorously validated against a separate, independent dataset of 221 points stratified on class types from the 2-m C-CAP high resolution landcover map with flooding cover identified from the 0.15-m resolution aerial photos taken on September 24, 2017 (NOAA Hurricane Maria Imagery, https://storms.ngs.noaa.gov/storms/maria/index.html). If an area showed flooding on the images taken on Sep. 24, 2017, the area was also assumed flooding on Sep. 21 and 22, 2017, i.e., one day and two days, respectively, right after the passage of Hurricane Maria with the images available.

Detecting water under tree canopies is usually done with L-band SAR (Hess et al. 1990). SAR images acquired at C-band have limited capacity to

penetrating canopies (Lehmann et al. 2015). There are studies using the widely available C band combined with optical bands based on the theory of double bouncing from water under canopies (Tsyganskaya et al. 2018; Gašparović and Klobučar 2021). However, this approach may not be appropriate for the case of mangroves with dense canopy, moreover, clear optical-band images were also rare because of clouds during the hurricanes. To estimate the flood under mangrove canopies without L-band data, we referenced the surrounding surface flood of large mangrove patches. Specifically, for every mangrove patch greater than 30 ha, the mean elevation of the surface flood within a 100-m buffer zone including the patch itself is used as the *flood height* of the mangrove patch. The 100-m buffer was chosen to include enough surface flooding pixels surrounding the target mangrove patch. Using the mean elevation reduced the effects of possible inaccuracy in DEM (with a vertical accuracy of 9.4 cm) and the effect of locally stagnant water on flood height, but on the other hand, provided a conservative estimation of flooding under mangrove canopies. For each big mangrove patch, pixels with elevation lower than the flood height were regarded as flooded. The flood height is a synthetic index that integrates all causal factors contributing to inundation, including tides, storm surging, and huge rainfall. The flood height may differ among the big mangrove patches, reflecting the difference in storm surge, rainfall, and drainage across the northern coast. For flooded pixels within each large mangrove patch, the calculation of flood depth as the difference between the flood height and the pixel elevation was applied to the dates of Sep. 21 and 28, 2017.

Impacts of inundation on mangroves' response to major hurricanes

To assess the impact of inundation on the response of mangroves to the major hurricanes, we used the enhanced vegetation index (EVI) (Huete et al. 2002) from Sentinel-2 images (Chastain et al. 2019; Yu and Gao 2020a) to represent the change in mangrove greenness before and after the major hurricanes. EVI is more sensitive to changes in greenness for high leaf biomass, and thus is more suitable for tropics than NDVI (Huete et al 2002). We used the dataset of Sentinel-2 MultiSpectral Instrument (MSI), Level-1C, archived at the Google Earth Engine, and preprocessed the data to mask the clouds and the shadows (Gorelick et al. 2017). We randomly chose pixels of 50 m by 50 m from the large mangrove patches to investigate the impacts of the hurricanes on the mangrove greenness in 2017 and the subsequent recovery till the end of 2021. For reference, we incorporated the mangrove greenness one year before the hurricanes, i.e., Sep. 6, 2016–Sep. 5, 2017, for comparison. Therefore, we extracted the time series of EVI for these pixels for the total period of Sep. 6, 2016–Dec. 31, 2021 and further smoothed the time series with a moving window of 45 days. The wide moving window was intended to reduce noise in raw EVI data. We first calculated the pre-hurricane EVI for reference, V_b, as the mean EVI during one year before the major hurricanes (Sep. 6, 2016–Sep. 5, 2017), and the minimum EVI immediately after the hurricanes within the period of Sep. 6–Dec. 31, 2017, $V_{\min}$, which indicates the lowest greenness due to the hurricanes and the post-hurricane drought (Miller et al. 2019; Yu and Gao 2020b). Then, to investigate the impacts, we calculated the relative impact of the hurricanes on EVI, I_r, as the reduction in the greenness divided by the reference greenness:

$$I_r = \frac{V_b - V_{min}}{V_b} \tag{1}$$

The higher the I_r, the more reduction in greenness and damage of the mangroves.

To investigate the recovery, we further calculated the recovery ratio after the hurricanes, R_r, as the ratio of the maximum annual mean EVI during 2020–2021 over the mean before the hurricanes (V_b), i.e., the reference greenness.

$$R_r = \frac{\max(V_{2020}, V_{2021})}{V_b} \tag{2}$$

where V_{2020} and V_{2021} are the annual mean EVI of 2020 and 2021, respectively. The lower the R_r, the more likely the mangrove mortality, while the higher the R_r, the stronger the mangrove recovery.

Finally, to explain the impact and the recovery after the hurricanes we applied spatial error models (Anselin and Griffith 1988) to regress the I_r and the R_r on the interpolated gust speed and rainfall during the hurricane, elevation, slope, and distance-to-nearest rivers/canals (Yu and Gao 2020b; Gao and Yu 2022), as well as the derived flood depths. The interpolated

Table 1 Error Matrix of the classification on the images of September 22, 2017 and error matrix of the classification for Sep. 21, 2017 shown in the parentheses

	Reference Data on Sep. 22, 2017 (Sep. 21, 2017)						User's Accuracy
	Permanent Water	Flooding	Mangroves	Herbaceous Cover	Upland Forest	Urban Cover	
Classified data							
Permanent water	**36 (30)**						1 (1)
Flooding		**39 (26)**					1 (1)
Mangroves			**32 (29)**	8 (6)	3 (2)	1 (1)	0.73 (0.76)
Herbaceous cover			3 (2)	**46 (43)**	3 (3)	6 (2)	0.79 (0.86)
Upland forest			1 (3)	2 (5)	**13 (9)**	4 (5)	0.65 (0.41)
Urban cover				3	1	**20 (20)**	0.83 (1.00)
Producer's Accuracy	1 (1)	1 (1)	0.89 (0.85)	0.78 (0.80)	0.65 (0.64)	0.65 (0.71)	**0.84 (0.84)**
Kappa Statistic							**0.81 (0.81)**

gust speed ranged from 43.8 to 46.4 m s^{-1} and the interpolated rainfall ranged in 143–572 mm in the study area with the highest gust speed and rainfall towards the hurricane path in the western part (Yu and Gao 2020b). Most of the study areas are in the right side of the hurricane path and experienced the strongest winds coming from the southeast. For reference, the normal rainfall in the study areas ranged from 1586 to 2159 mm annually with the highest rainfall in the eastern part (Yu and Gao 2020b). For the area close to the hurricane path in the west, the hurricane-induced rainfall almost counts for one third of the normal annual rainfall. We iteratively selected the explanatory variables according to the minimum AIC (Akaike Information Criterion), a widely accepted index that balances model complexity and likelihood of the model fit to the data. We first fit a full model with all the independent variables. By iteration, we then gradually eliminated the variable meeting the following criteria: the variable is not significant and dropping the variable could lead to a biggest decrease in AIC.

Results

Classification accuracy with respect to the high-resolution aerial photos

According to the independent validation dataset derived from the high-resolution aerial photos, all permanent water and surface flood points are correctly identified with 100% accuracy (Table 1). Therefore, our analysis shows that the SAR C-band from Sentinel-1 has consistent high capability to recognize water-related pixels. The overall accuracy on six land cover types reached 0.84 with a kappa statistic of 0.81 (Table 1). The non-water points are classified with lower accuracies. For the image classification on Sep. 22, 2017, the omission error for mangroves and associates is 11%, and the upland forests, the land cover type with the lowest accuracy, are mostly confused with mangroves and herbaceous cover with both omission and commission errors of 35%.

Spatial and temporal extent of surface flood at the coastal wetlands

Applying the classification model, we found large, inundated areas along the coast on Sep. 21, 2017, one day after Hurricane Maria (Fig. 2). The marshes and grasslands located east of Rio Grande del Loiza (Fig. 2), near Rio de la Plata, near Rio Cibuco and Cibuco natural reserve, and near Rio Grande de Manati were mostly flooded. In total, 4399 ha, including 22% palustrine marshes, in the study area were flooded on Sep 21, 2017. The total flooded surface decreased to 2042 ha on Sep. 22, 2017 (−54%, Fig. 3), and the map of Sep. 22 shows that the areas near Rio de la Plata and near Rio Cibuco (Fig. 2) were still flooded. Surface flood in the palustrine wetlands reduced from 1496 to 635 ha (−58%), that in the estuarine wetlands declined from 132 to 52 ha

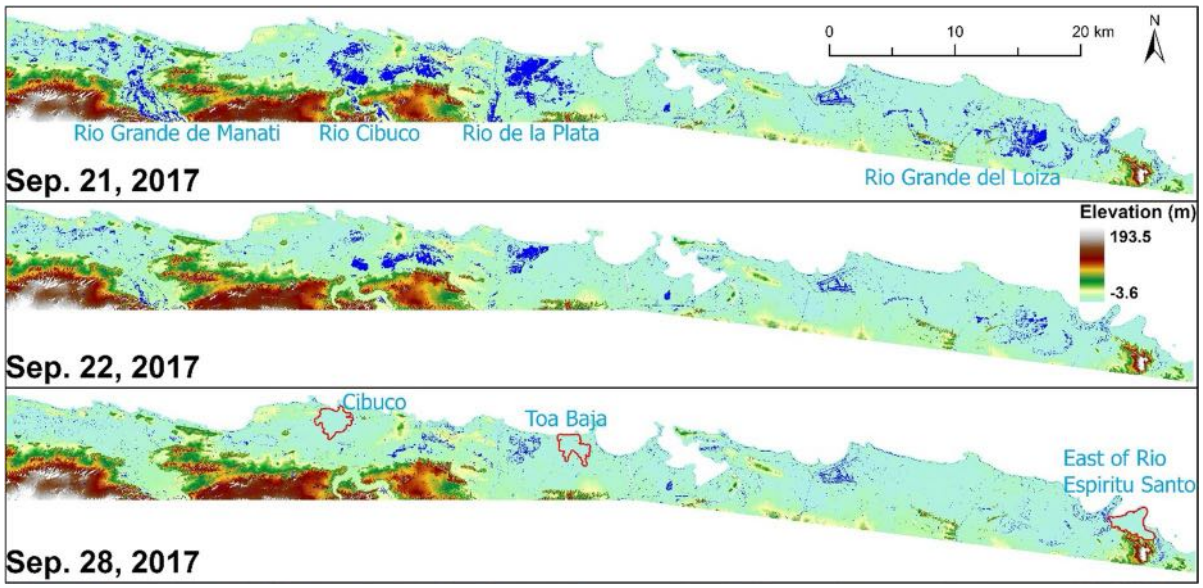

Fig. 2 Detected surface flood (in blue) in the northern coast on Sep. 21, Sep. 22, and Sep. 28, 2017. The background is the elevation profile in the area

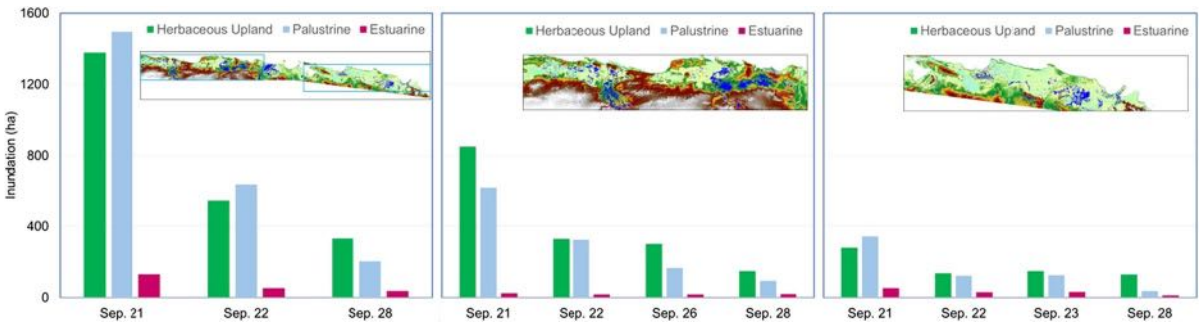

Fig. 3 Detected surface flooded areas (in ha) in the northern coast on Sep. 21, 22, and 28, 2017 (left), in the western part on Sep. 21, 22, 26, and 28, 2017 (middle), and in the eastern part on Sep. 21, 22, 23, and 28, 2017 (right)

(−61%), and that in herbaceous uplands changed from 1377 to 544 ha (−60%) from Sep. 21 to Sep. 22, 2017.

Two additional images were available with one covering the eastern part on Sep. 23 and the other covering the western part on Sep. 26, 2017 (Online Appendix 1), which showed continuous reducing of surface flood in palustrine wetlands (Fig. 3). Surface flooded areas kept shrinking (Fig. 2) and on Sep. 28 the total detected surface flood was 1379 ha (−69% from that on Sep. 21, 2017) with 204 ha in palustrine wetlands (−86%) and 36 ha in estuarine wetlands (−73%) (Fig. 3).

Flood depth under mangroves

Based on the detected surface flood around mangrove patches, the estimation of flood under mangroves showed spatial heterogeneity across the large mangrove patches (Fig. 4). For example, the estimation of flood depth under mangroves on Sep. 28, 2017 at Cibuco Natural Reserve ranges from 0 to 0.68 m with a mean and a standard deviation as 0.07 ± 0.06 m. The estimated flood depth under the mangroves in the northern Toa Baja ranges in 0–0.42 m with a mean of 0.1 ± 0.06 m. Compared to the above two sites, the estimated flood depth

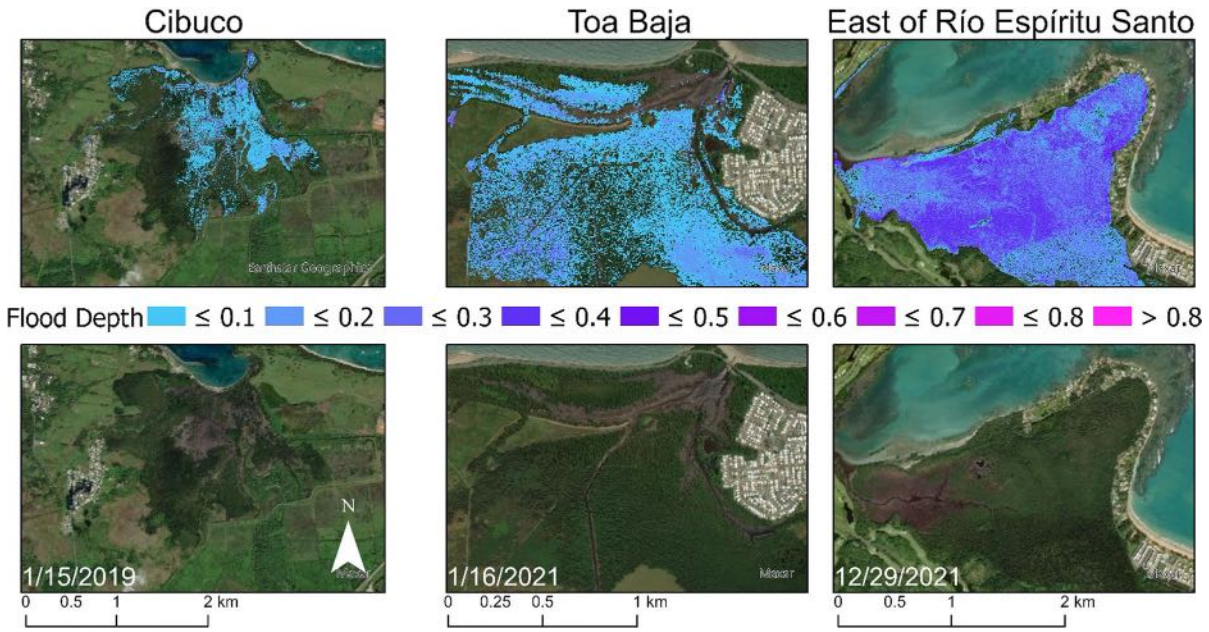

Fig. 4 Estimated flood depth (m) under mangroves on Sep. 28, 2017 (upper panel) based on the surface inundation detected in the immediate neighborhoods of mangroves near Cibuco Natural Reserve, northern Toa Baja, and east of Rio Espiritu Santo. Recent images of the areas (lower panel) showed the mangroves that failed to recover (brown patch) after the hurricanes

under the mangroves east of the Rio Espiritu Santo is much higher with a mean of 0.23 ± 0.09 m and a maximum of 0.77 m. Recent high-resolution images also showed that some mangroves failed to recover at these sites (Fig. 4 lower panel, brown places. Image date: 1/15/2019 for Cibuco, 1/16/2021 for Toa Baja, and 12/29/2021 for East of Rio Espiritu Santo).

Impacts of inundation on mangroves' response to major hurricanes

We calculated the relative impact index and the recovery ratio for the spatially sampled pixels which resulted in the mean of 0.52 ± 1.5 and the range of 0.07–0.85 for I_r and the mean of 0.93 ± 0.23 and the range from 0.25 to 1.47 for R_r. The EVI dynamics of each sampled pixel can be classified into three general types depending on the recovery status: over recovery with recovery ratio ≥ 1, partial recovery with an $R_r \geq 0.5$ but < 1, and little recovery with an $R_r < 0.5$ (Fig. 5). About 43% of the sampled pixels fall into the over recovery category, 49% in partial recovery, and 8% in little recovery (Fig. 6).

The regression of the relative impact index, I_r, the dependent variable in Eq. 1 (Fig. 5, $(V_b\text{-}V_{min})/V_b$) showed significant effects of the hurricane wind and the topography:

$$I_r = 0.535 + 0.175w - 0.322z \quad (3)$$

where w is the normalized gust windspeed during the hurricane and z is the normalized elevation. The p-value for the gust windspeed is 0.016 and the p-value for the elevation is 0.0001. The regression has a spatial autocorrelation coefficient λ of 0.65 and an r^2 of 0.25. Hence the higher the gust windspeed and/or the lower the elevation, the more reduction in EVI of the mangroves and the higher the relative impact.

The regression of the recovery ratio, R_r, with the spatial error model resulted in the following equation:

$$R_r = 1.232 - 0.163p - 0.392I_r - 0.145d_{28} \quad (4)$$

where p is the normalized total rainfall during the hurricane, and d_{28} is the normalized derived flood depth on Sep. 28, 2017. The p-values for the

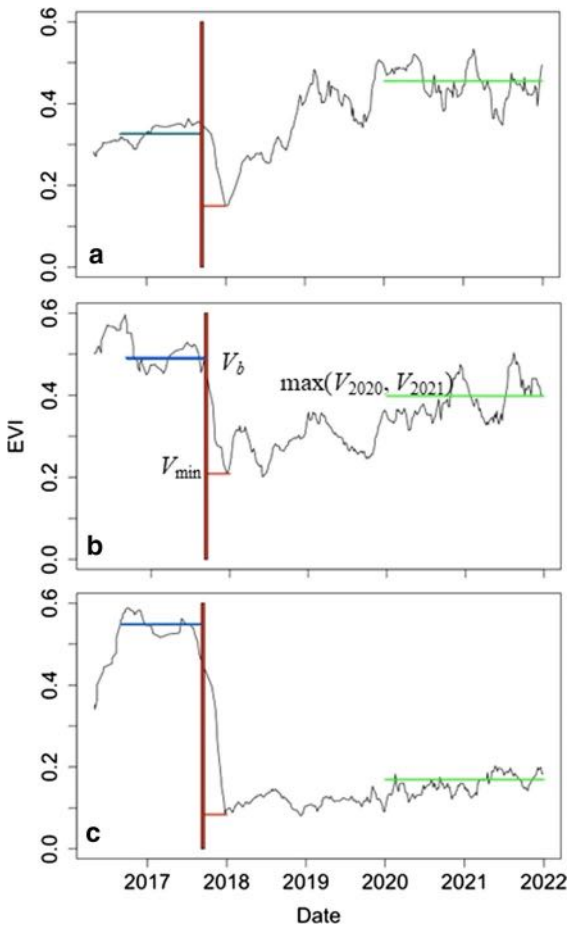

Fig. 5 Examples of the EVI dynamics for spatially sampled pixels**.** The red vertical bar stands for the hurricane period starting from Sep. 6 to Sep. 20, 2017. The blue horizontal line to the left of the red bar indicates the one year mean EVI from Sep. 6, 2016 to Sep. 5, 2017 (V_b) before the hurricanes. The short red horizontal line indicates the minimum EVI right after the hurricanes until Dec. 31, 2017 ($V_{\min}$). The green horizontal line represents the maximum of the annual means of the EVI in 2020 and 2021 ($\max(V_{2020}, V_{2021})$). Panels a, b, and c represent the categories of over, partial, and little recovery, defined as $R_r \geq 1$, $1 > R_r \geq 0.5$, and $R_r < 0.5$, respectively

hurricane rainfall, the relative impact, and the flood depth are 0.094, < 0.001, and 0.021, respectively. The regression has a spatial autocorrelation coefficient λ of 0.82 and an r^2 of 0.54. Therefore, the more damage to the mangroves (I_r, impact), the severer the inundation (d_{28}, prolonged inundation depth), and/or the higher the hurricane rainfall (p), the less the recovery of the mangroves. The predicted versus the observed recovery ratio showed potential overestimation when

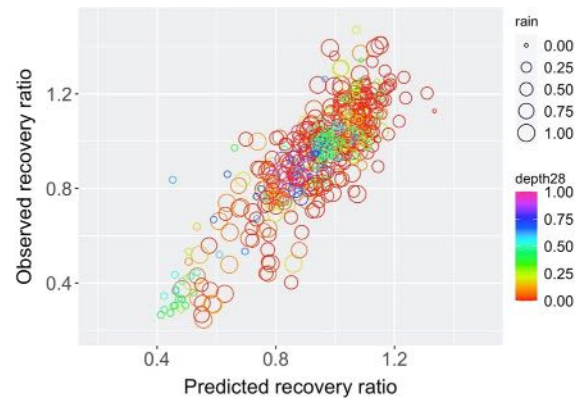

Fig. 6 Observed versus predicted recovery ratio resulted from a spatial error model. Rain indicated the total hurricane rainfall and depth28 indicated the derived flood depth on September 28, 2017

the observed ratio is below 0.4 and underestimation when the observed ratio is above 1.2 (Fig. 6). The chart showed a gap around the recovery ratio in the range of 0.4–0.5 and the points with the observed R_r below that had little recovery.

Discussion

Inundation, hurricane impact, and recovery

While L-band SAR images are not available to assess the inundation under mangrove canopies (Hess et al. 1990) after the two mega hurricanes with the frequency of once every 100 years, we used a two-step approach of detecting surface floods based on the available C-band SAR (Huang et al. 2018; Jiang et al. 2021) and then deriving the floods under canopies by referencing the surrounding surface floods. The first step has been demonstrated with high accuracy, whereas using the mean elevation of the surrounding surface floods as the flood height to derive the floods under mangrove canopies may be subject to uncertainty. The flood depth was based on the elevation but is not equivalent to elevation. Replacing the flooding depth (d_{28}) with elevation in the right hand of the regression equation of Eq. 4 reduced r^2 and increased the Akaike Information Criterion, therefore, the flooding depth turned out to be a better explainer than elevation in the mangrove recovery after the major hurricanes.

We also derived the spatial patterns of the hurricane impact and the 4-year recovery based on the satellite-measured greenness. Our EVI-based impact and recovery might be affected by a severe drought before the hurricanes (Herrera and Ault 2017; Mote et al. 2017). Puerto Rico experienced a severe and prolonged drought during 2014–2016, and the years of 2017–2021 are not regarded as dry years (Online Appendix 2). The drought reduced freshwater supply to the wetlands and increased the salinity, and thus decreased greenness. Should the annual rainfall in 2014–2016 be normal, the reference EVI before the hurricane (V_b) would have been large. If we assume the minimum EVI right after the hurricane ($V_{\min}$) does not change too much, then the relative impact, I_r ($(V_b - V_{\min})/V_b = 1 - V_{\min}/V_b$), would have increased with a larger V_b, thus the mean impact would have been larger than 0.52. Similarly, the calculated average recovery of 0.93 is also affected by the lower before-hurricane EVI. The cases with a recovery ratio greater than 1 (43%) can be attributed to this climate variation. When sufficient rainfall came after the hurricanes, the annual mean EVI might exceed that before the hurricanes. The EVI-based recovery in 4 years mostly reflects the recovery of leaves and mangrove functions with respect to carbon assimilation, transpiration, and gas regulation. The recovery of other functions and ecosystem structure may take much longer time (Beard et al. 2005; Lugo 2008).

Variables contributing to the impact and the recovery

Hurricane wind is believed to be a dominant driver for forest canopy damage (Mitchell 2012; Gardiner et al. 2019; Gao and Yu 2021a). The LiDAR-based 3-D canopy structure studies showed that, in addition to gust speed, the canopy height reduction of mangroves at multiple sites is also significantly enlarged by the rainfall during the hurricanes (Gao and Yu 2022). In a short term right after the hurricanes, the EVI-based greenness in this study (Eq. 3) was not significantly affected by the hurricane rainfall which was probably because of the limitation of the 2-D detection with optical bands.

More impacts at lower elevation have been found in the existing studies in Puerto Rico and South Florida (Yu and Gao 2020b; Lagomasino et al. 2021; Gao and Yu 2022). Mangrove at lower elevation receives more freshwater and nutrients from the nearby freshwater and sewage canals than those at higher elevation, which changes the allocation pattern. More shoot growth with better nutrient and lower salinity but less root-soil anchorage in muddier soil makes the mangroves at lower elevation easy to be raptured and uprooted (Gao and Yu 2021b). This study confirms the findings about the role of elevation in mangrove damages using the optical and LiDAR images.

The ratio of recovery of mangrove ecosystems from hurricane disturbance depends heavily on the severity of impact (Asbridge et al. 2018). In this study, the relative impact appeared as the most significant explanatory factor in the regression of recovery (Eq. 4). The regrowth gets slower as the initial damage increases from partial defoliation to ruptured branches/stems to uprooting, so does the remotely-sensed recovery ratio (Herrera-Silveira et al. 2022).

Flood depth determines the proportion of the aerial roots under water, thus inhibiting respiration of mangroves (Choy and Booth 1994). The flood depth derived from the high-resolution DEM right before the major hurricanes provided a synergistic effect of inundation and mud smothering. The larger the proportion of the aerial roots under water, the more delayed damage or dieback. The prolonged inundation depth is significant in explaining mangrove mortality and recovery. The prolonged inundation depth reflects both temporal span of flooding and difference in elevation which emphasizes cross-site spatial heterogeneity in topography. It is worth pointing out that the flood depth variable of d_{28} in Eq. 4 may bear more information than the one-week inundation. The flood may last more than one week at those places with lower elevation, and the flood may also be associated with various amount of mud deposit as found in those field studies in Florida (Radabaugh et al. 2020). Although the mud deposit benefits accretion to offset sea level rise (Clough et al. 2016), the inundation and mud deposit may smother the aerial roots and lead to dieback and mortality, and the death of mangroves may cause peat collapse and reduce the accretion due to mud deposit (Cahoon et al. 2003).

Rainfall is one of the major causes of inundation, together with storm surge to induce compound flooding of oceanic, fluvial, and pluvial ones (Ye et al. 2021). The effect of rainfall should have been represented by the flood depth. The reason that rainfall still appears significant in explaining mangrove recovery

might be that the rainfall, to some degree, compensates for the inaccuracy involved in the derived flood depth pattern.

Recovery of a system after disturbance also depends on the pertinent internal characteristics of the system. The spatial error model only explained 54% of the observed recovery. The internal characteristics plus localized environments should explain most of the remaining. Much of the severe damage or mortality happened at lower elevation (Fig. 4). The slow recovery mostly happened at lower elevation where red and black mangroves reside. Localized environmental conditions such as hydrology, salinity, and available nutrients also affect the regrowth and recovery. The red mangroves, living near coast or lagoon/river, have lower wood density, which makes the stems and branches of the species easier to be ruptured (Asbridge et al. 2018; Herrera-Silveira et al. 2022). The root structure of black mangroves makes it prone to flooding damage (Lovelock et al. 2016). *Avicennia* species have less root cap and delayed vesicular development than other species. Water and salts are easier to enter the plant of *Avicennia* species (Lovelock et al. 2016). Also, the aerial roots of black mangroves (Pneumatophores) are near ground surface and easily to be immersed.

In addition to the apparent effects on the calculations of the impact and the recovery indices, pre-hurricane drought may have legacy on the responses of mangroves to hurricanes and subsequent recovery. Drought events were associated with high salinity due to reduced freshwater supply and enhanced evapotranspiration, which caused mangrove mortality and reduced recruitment of seedlings (Yu et al. 2019), thus reduced the density of the mangrove canopy. Previous studies showed that tree density is important for forests to resist wind damage (Gardiner et al. 2008; Jimenez-Rodríguez et al. 2018). Therefore, lower tree density is associated with greater wind damage. The lower tree density caused by pre-hurricane drought tends to be associated with greater wind damage.

Limitation and future remote-sensed inundation

Recent advances in all-weather, cloud-penetrating, moderate-resolution SAR images with frequent revisits greatly improve the possibility of in-time flood monitoring in rapid response to natural disasters (Nemni et al. 2020; Jiang et al. 2021), and the application of machine learning ensured high accuracy in identifying flooding patches (Hosseini et al. 2020; Nemni et al. 2020). For example, random forest classification algorithm was applied to automatically extract surface water extent in both prairie and coastal wetlands of US using the Sentinel-1 C-band SAR (Huang et al. 2018), and the overall accuracy was ranging from 82 to 93% with kappa statistics around 0.64–0.84. Using random forest classification, the accuracy of this study reached an overall accuracy of 0.84 and a kappa statistics of 0.81 when including all the land cover types, and particularly, the detection of surface flood or permanent water was very successful. Although Normalized Difference Flood in short Vegetation Index (NDFVI) was proposed to detect double bouncing effects of the backscatters from the shallow water under short vegetation (Cian et al. 2018a), in our study areas, the average canopy heights are above 10 m, and the calculated NDFVI according to the difference of backscatters between the flood event and the reference period at C-band did not work well to directly detect water under the canopies. The derived flood depth based on the DEM acquired right before the hurricanes reflects the synergetic effects of stagnant water and possible mud deposition (Radabaugh et al. 2020). Possible scouring due to the hurricanes might lead to actually deeper flooding than the estimation but won't change the proportion of aerial roots that was above the flood height and able to respirate. Due to the scale of the mud deposits (Radabaugh et al. 2020), current vertical accuracies of the DEM acquired before and after the hurricanes, i.e., 9.4 cm versus 6.8 cm, would not support a rigorous analysis to separate the effects of mud deposition.

Recent study of joint hazards of hurricane-induced rainfall and storm surge emphasized far more frequent extreme floodings in the southern and eastern US coasts when combined with rising sea level (Gori et al. 2022). This would lead to more severe inundation and mangrove dieback. Compared to the C-band SAR images, L-band SAR has better canopy penetrating capability and also higher correlation with the in-situ flood depth as proved in the freshwater marsh in Everglades, Florida, US (Kim et al. 2014). Future L-band SAR with frequent revisits, such as NISAR (NASA-ISRO Synthetic Aperture Radar) scheduled to launch in January 2024, will greatly improve the capability of flood detection under mangroves and flood depth estimation. It would be promising to

integrate tropical cyclones (Krauss and Osland 2019; Gao and Yu 2022), lengthy drought (Duke et al. 2017), and sea level rise (Krauss et al. 2014; Lovelock et al. 2015) into future studies of mangroves' responses to climate changes.

Author contributions All authors contributed to the study conception and design. Material preparation, data collection and analysis were performed by MY and QG. The first draft of the manuscript was written by MY and all authors commented on previous versions of the manuscript. All authors read and approved the final manuscript.

Funding This work was supported by the NOAA Sea Grant (Grant number NA18OAR4170089).

Data availability All the datasets analysed are publicly available at the websites of NOAA Hurricane Maria Imagery, https://storms.ngs.noaa.gov/storms/maria/index.html, NOAA Data Access Viewer with DEM and Land Cover maps, https://coast.noaa.gov/dataviewer/#/, and Sentinel images, https://developers.google.com/earth-engine/datasets/catalog/COPERNICUS_S1_GRD?hl=en.

Declarations

Competing interests The authors have no relevant financial or non-financial interests to disclose.

References

Anderson SM, Ury EA, Taillie PJ et al (2022) Salinity thresholds for understory plants in coastal wetlands. Plant Ecol 223:323–337

Anselin L, Griffith DA (1988) Do spatial effects really matter in regression analysis? Pap Reg Sci 65(1):11–34

Asbridge E, Lucas R, Rogers K, Accad A (2018) The extent of mangrove change and potential for recovery following severe Tropical Cyclone Yasi, Hinchinbrook Island, Queensland, Australia. Ecol Evol 8(21):10416–10434

Barbier EB, Hacker SD, Kennedy C, Koch EW, Stier AC, Silliman BR (2011) The value of estuarine and coastal ecosystem services. Ecol Monogr 81(2):169–193

Bartsch A, Wagner W, Scipal K, Pathe C, Sabel D, Wolski P (2009) Global monitoring of wetlands - the value of ENVISAT ASAR Global mode. J Environ Manag 90(7):2226–2233

Beard KH, Vogt KA, Vogt DJ et al (2005) Structural and functional responses of a subtropical forest to 10 years of hurricanes and droughts. Ecol Monogr 75(3):345–361

Breiman L (2001) Random forests. Mach Learn 45(1):5–32

Cahoon DR, Hensel P, Rybczyk J, McKee KL, Proffitt CE, Perez BC (2003) Mass tree mortality leads to mangrove peat collapse at Bay Islands, Honduras after Hurricane Mitch. J Ecol 91(6):1093–1105

Chastain R, Housman I, Goldstein J, Finco M, Tenneson K (2019) Empirical cross sensor comparison of Sentinel-2A and 2B MSI, Landsat-8 OLI, and Landsat-7 ETM+ top of atmosphere spectral characteristics over the conterminous United States. Remote Sens Environ 221:274–285

Chen B, Xiao X, Li X et al (2017) A mangrove forest map of China in 2015: analysis of time series Landsat 7/8 and Sentinel-1A imagery in Google Earth Engine cloud computing platform. ISPRS J Photogramm Remote Sens 131(Supplement C):104–120

Choy SC, Booth WE (1994) Prolonged inundation and ecological changes in an Avicennia mangrove: implications for conservation and management. Hydrobiologia 285(1):237–247

Cian F, Marconcini M, Ceccato P (2018a) Normalized difference flood index for rapid flood mapping: taking advantage of EO big data. Remote Sens Environ 209:712–730

Cian F, Marconcini M, Ceccato P, Giupponi C (2018b) Flood depth estimation by means of high-resolution SAR images and lidar data. Nat Hazards Earth Syst Sci 18(11):3063–3084

Clement MA, Kilsby CG, Moore P (2018) Multi-temporal synthetic aperture radar flood mapping using change detection. J Flood Risk Manag 11(2):152–168

Clough J, Polaczyk A, Propato M (2016) Modeling the potential effects of sea-level rise on the coast of New York: integrating mechanistic accretion and stochastic uncertainty. Environ Model Softw 84:349–362

Costanza R, Pérez-Maqueo O, Martinez ML, Sutton P, Anderson SJ, Mulder K (2008) The value of coastal wetlands for hurricane protection. Ambio 37(4):241–248

Dahl TE, Stedman SM (2013) Status and trends of wetlands in the coastal watersheds of the Conterminous United States 2004 to 2009. U.S. Department of the Interior, Fish and Wildlife Service and National Oceanic and Atmospheric Administration, National Marine Fisheries Service, p 46

Duke NC, Kovacs JM, Griffiths AD et al (2017) Large-scale dieback of mangroves in Australia's Gulf of Carpentaria: a severe ecosystem response, coincidental with an unusually extreme weather event. Mar Freshw Res 68(10):1816–1829

Ellison JC (1999) Impacts of sediment burial on mangroves. Mar Pollut Bull 37(8):420–426

Gao Q, Yu M (2014) Discerning fragmentation dynamics of tropical forest and wetland during reforestation, urban sprawl, and policy shifts. PLoS ONE 9(11):e113140

Gao Q, Yu M (2021a) Canopy density and roughness differentiate resistance of a tropical dry forest to major hurricane damage. Remote Sens 13(12):2262

Gao Q, Yu M (2021b) Elevation and distribution of freshwater and sewage canals regulate canopy structure and differentiate hurricane damages to a basin mangrove forest. Remote Sens 13(17):3387

Gao Q, Yu M (2022) Elevation regimes modulated the responses of canopy structure of coastal mangrove forests to hurricane damage. Remote Sens 14(6):1497

Gardiner B, Byrne K, Hale S et al (2008) A review of mechanistic modelling of wind damage risk to forests. Forestry 81(3):447–463

Gardiner B, Achim A, Nicoll B, Ruel J-C (2019) Understanding the interactions between wind and trees: an introduction to the IUFRO 8th Wind and Trees Conference (2017). Forestry 92(4):375–380

Gašparović M, Klobučar D (2021) Mapping floods in lowland forest using sentinel-1 and sentinel-2 data and an object-based approach. Forests 12(5):553

Gedan KB, Kirwan ML, Wolanski E, Barbier EB, Silliman BR (2011) The present and future role of coastal wetland vegetation in protecting shorelines: answering recent challenges to the paradigm. Clim Change 106(1):7–29

Gorelick N, Hancher M, Dixon M, Ilyushchenko S, Thau D, Moore R (2017) Google earth engine: planetary-scale geospatial analysis for everyone. Remote Sens Environ 202:18–27

Gori A, Lin N, Xi D, Emanuel K (2022) Tropical cyclone climatology change greatly exacerbates US extreme rainfall–surge hazard. Nat Clim Change 12(2):171–178

Han X, Feng L, Hu C, Kramer P (2018) Hurricane-induced changes in the everglades National Park Mangrove Forest: landsat observations between 1985 and 2017. J Geophys Res Biogeosci 123(11):3470–3488

Herrera D, Ault T (2017) Insights from a new high-resolution drought atlas for the Caribbean spanning 1950–2016. J Clim 30(19):7801–7825

Herrera-Silveira JA, Teutli-Hernandez C, Secaira-Fajardo F et al (2022) Hurricane damages to mangrove forests and post-storm restoration techniques and costs. The Nature Conservancy, The Nature Conservancy, Arlington

Hess LL, Melack JM, Simonett DS (1990) Radar detection of flooding beneath the forest canopy: a review. Int J Remote Sens 11(7):1313–1325

Hoekman DH, Reiche J (2015) Multi-model radiometric slope correction of SAR images of complex terrain using a two-stage semi-empirical approach. Remote Sens Environ 156:1–10

Hosseini FS, Choubin B, Mosavi A et al (2020) Flash-flood hazard assessment using ensembles and Bayesian-based machine learning models: application of the simulated annealing feature selection method. Sci Total Environ 711:135161

Huang C, Peng Y, Lang M, Yeo I-Y, McCarty G (2014) Wetland inundation mapping and change monitoring using Landsat and airborne LiDAR data. Remote Sens Environ 141:231–242

Huang W, DeVries B, Huang C et al (2018) Automated extraction of surface water extent from sentinel-1 data. Remote Sens 10(5):797

Huete A, Didan K, Miura T, Rodriguez EP, Gao X, Ferreira LG (2002) Overview of the radiometric and biophysical performance of the MODIS vegetation indices. Remote Sens Environ 83(1–2):195–213

Hughes KS, Schulz W (2020) Map depicting susceptibility to landslides triggered by intense rainfall, Puerto Rico. U.S. Geological Survey Open-File Report 2020–1022, Reston

Imbert D (2018) Hurricane disturbance and forest dynamics in east Caribbean mangroves. Ecosphere 9(7):e02231

Jiang X, Liang S, He X et al (2021) Rapid and large-scale mapping of flood inundation via integrating spaceborne synthetic aperture radar imagery with unsupervised deep learning. ISPRS J Photogramm Remote Sens 178:36–50

Jimenez JA, Lugo AE, Cintron G (1985) Tree mortality in mangrove forests. Biotropica 17(3):177–185

Jimenez-Rodríguez DL, Alvarez-Añorve MY, Pineda-Cortes M et al (2018) Structural and functional traits predict short term response of tropical dry forests to a high intensity hurricane. For Ecol Manag 426:101–114

Kennaway T, Helmer EH (2007) The forest types and ages cleared for land development in Puerto Rico. Gisci Remote Sens 44:356–382

Kim J-W, Lu Z, Jones JW, Shum CK, Lee H, Jia Y (2014) Monitoring Everglades freshwater marsh water level using L-band synthetic aperture radar backscatter. Remote Sens Environ 150:66–81

Kirwan ML, Megonigal JP (2013) Tidal wetland stability in the face of human impacts and sea-level rise. Nature 504(7478):53–60

Krauss KW, Osland MJ (2019) Tropical cyclones and the organization of mangrove forests: a review. Ann Bot 125(2):213–234

Krauss KW, McKee KL, Lovelock CE et al (2014) How mangrove forests adjust to rising sea level. New Phytol 202(1):19–34

Lagomasino D, Fatoyinbo T, Castañeda-Moya E et al (2021) Storm surge and ponding explain mangrove dieback in southwest Florida following Hurricane Irma. Nat Commun 12(1):4003

Lehmann EA, Caccetta P, Lowell K et al (2015) SAR and optical remote sensing: assessment of complementarity and interoperability in the context of a large-scale operational forest monitoring system. Remote Sens Environ 156:335–348

Lewis RR, Milbrandt EC, Brown B et al (2016) Stress in mangrove forests: early detection and preemptive rehabilitation are essential for future successful worldwide mangrove forest management. Mar Pollut Bull 109(2):764–771

López-Marrero T, Heartsill-Scalley T, Rivera-López CF, Escalera-García IA, Echevarría-Ramos M (2019) Broadening our understanding of hurricanes and forests on the Caribbean Island of Puerto Rico: where and what should we study now? Forests 10(9):710

Lovelock CE, Cahoon DR, Friess DA et al (2015) The vulnerability of Indo-Pacific mangrove forests to sea-level rise. Nature 526(7574):559–563

Lovelock CE, Krauss KW, Osland MJ, Reef R, Ball MC (2016) The physiology of mangrove trees with changing climate. In: Goldstein G, Santiago LS (eds) Tropical tree physiology: adaptations and responses in a changing environment. Springer, Cham, pp 149–179

Lugo AE (2008) Visible and invisible effects of hurricanes on forest ecosystems: an international review. Austral Ecol 33(4):368–398

Martinuzzi S, Gould WA, Lugo AE, Medina E (2009) Conversion and recovery of Puerto Rican mangroves: 200 years of change. For Ecol Manag 257(1):75–84

Miller PW, Kumar A, Mote TL, Moraes FDS, Mishra DR (2019) Persistent hydrological consequences of hurricane Maria in Puerto Rico. Geophys Res Lett 46(3):1413–1422

Miller GL, Lugo AE (2009) Guide to the ecological systems of Puerto Rico. Gen. Tech. Rep. IITF-GTR-35. U.S. Department of Agriculture, Forest Service, International Institute of Tropical Forestry, San Juan, PR, p 437

Mitchell SJ (2012) Wind as a natural disturbance agent in forests: a synthesis. Forestry 86(2):147–157
Mote TL, Ramseyer CA, Miller PW (2017) The Saharan air layer as an early rainfall season suppressant in the Eastern Caribbean: the 2015 Puerto Rico Drought. J Geophys Res 122(20):10966–10982
Nemni E, Bullock J, Belabbes S, Bromley L (2020) Fully convolutional neural network for rapid flood segmentation in synthetic aperture radar imagery. Remote Sens 12(16):2532
Office for Coastal Management (2020) C-CAP Land Cover, Puerto Rico, 2010. https://www.fisheries.noaa.gov/inport/item/48301
Pasch RJ, Penny AB, Berg R (2019) National Hurricane Center Tropical Cyclone Report - Hurricane Maria (AL152017) September 16–30, 2017. National Hurricane Center, pp 1–48
Patrick CJ, Yeager L, Armitage AR et al (2020) A system level analysis of coastal ecosystem responses to hurricane impacts. Estuaries Coasts 43:943–959
Pekel J-F, Cottam A, Gorelick N, Belward AS (2016) High-resolution mapping of global surface water and its long-term changes. Nature 540(7633):418–422
Quadros AF, Zimmer M (2017) Dataset of "true mangroves" plant species traits. Biodivers Data J 5:e22089–e22089
Radabaugh KR, Moyer RP, Chappel AR et al (2020) Mangrove damage, delayed mortality, and early recovery following hurricane irma at two landfall sites in Southwest Florida, USA. Estuar Coasts 43(5):1104–1118
Singha M, Dong J, Sarmah S et al (2020) Identifying floods and flood-affected paddy rice fields in Bangladesh based on Sentinel-1 imagery and Google Earth Engine. ISPRS J Photogramm Remote Sens 166:278–293
Sippo JZ, Lovelock CE, Santos IR, Sanders CJ, Maher DT (2018) Mangrove mortality in a changing climate: an overview. Estuar Coast Shelf Sci 215:241–249
Taillie PJ, Roman-Cuesta R, Lagomasino D et al (2020) Widespread mangrove damage resulting from the 2017 Atlantic mega hurricane season. Environ Res Lett 15(6):064010
Torres R, Snoeij P, Geudtner D et al (2012) GMES Sentinel-1 mission. Remote Sens Environ 120:9–24
Tsyganskaya V, Martinis S, Marzahn P, Ludwig R (2018) SAR-based detection of flooded vegetation: a review of characteristics and approaches. Int J Remote Sens 39(8):2255–2293
Veloso A, Mermoz S, Bouvet A et al (2017) Understanding the temporal behavior of crops using Sentinel-1 and Sentinel-2-like data for agricultural applications. Remote Sens Environ 199:415–426
Vollrath A, Mullissa A, Reiche J (2020) Angular-based radiometric slope correction for sentinel-1 on google earth engine. Remote Sens 12(11) : 1867
Wadsworth FH, Englerth GH (1959) Effects of the 1956 hurricane on forests in Puerto Rico. Caribbean Forester 20(3/4):38–51
Wu Q, Lane CR, Li X et al (2019) Integrating LiDAR data and multi-temporal aerial imagery to map wetland inundation dynamics using Google Earth Engine. Remote Sens Environ 228:1–13
Ye F, Huang W, Zhang YJ et al (2021) A cross-scale study for compound flooding processes during Hurricane Florence. Nat Hazards Earth Syst Sci 21(6):1703–1719
Yu M, Gao Q (2020a) Increasing summer rainfall and asymmetrical diurnal and seasonal warming enhanced vegetation greenness in temperate deciduous forests and grasslands of Northern China. Remote Sens 12(16):2569
Yu M, Gao Q (2020b) Topography, drainage capability, and legacy of drought differentiate tropical ecosystem response to and recovery from major hurricanes. Environ Res Lett 15(10):104046
Yu M, Rivera-Ocasio E, Heartsill-Scalley T, Davila-Casanova D, Rios-López N, Gao Q (2019) Landscape-level consequences of rising sea-level on coastal wetlands: saltwater intrusion drives displacement and mortality in the twenty-first century. Wetlands 39(6):1343–1355